MAGNETODYNAMIC FORMULATION RESOLVING EDDY-CURRENT EFFECTS IN THE YOKE AND THE SUPERCONDUCTIVE CABLE OF THE FAIR DIPOLE MAGNETS*

H. De Gersem, S. Koch, T. Weiland,
Institut für Theorie Elektromagnetischer Felder, Technische Universität Darmstadt, Germany

Abstract

Transient 3D simulations are carried out for two types of superconductive dipole magnets. Eddy-current effects in the yoke are treated by homogenising the laminated iron composite whereas interstrand eddy-current effects are resolved by either a cable magnetization model or a cable eddy-current model. The simulations reveal the Joule losses in the magnets.

INTRODUCTION

Within the Facility for Antiproton and Ion Research (FAIR) at the Gesellschaft für Schwerionenforschung (GSI) in Darmstadt, two new synchrotrons, SIS-100 and SIS-300, are planned. Both will be equipped with superconductive dipole magnets in order to achieve higher magnetic flux densities and to reduce the operating cost [16, 10]. Typical for the installation is the relatively high ramping rate which amounts to 4 T/s for the SIS-100 dipole magnets. Substantial eddy-current effects are expected which may deteriorate the aperture-field quality and may cause excessive Joule losses. Eddy currents crossing the relatively low thermal and electric insulation between the cable strands cause a deterioration of the aperture field along the whole magnet length and can be computed by 2D finite-element models. Eddy currents appear at the end parts of the yoke due to axial magnetic flux components. They have less influence on the overall field quality but may introduce severe Joule losses. The quantification of these eddy-current effects requires a 3D model. In this paper, an appropriate, transient, nonlinear, 3D magnetodynamic formulation is proposed which deals with both eddy-current phenomena. Because of the axial lamination of the yoke parts and because of the geometrical details inside the superconductive coils, homogenization techniques have to be introduced in order to avoid the necessity of resolving small spatial scales in the computational grid.

TRANSIENT 3D MAGNETODYNAMIC FORMULATION

Effects related to the change of the electrical energy density can be neglected with respect to the effects corresponding to the change of the magnetic energy density and the loss density. Therefore, the displacement current density is omitted in Ampères law, yielding $\nabla \times \vec{H} = \vec{J}$ where $\vec{H}$ is the magnetic field strength and $\vec{J}$ is the current density. The magnetic flux density is $\vec{B} = \mu\vec{H}$ where μ is the permeability which depends on $\vec{B}$ and which may be anisotropic, e.g., due to the homogenization described below. The magnetic flux density is forced to be divergence-free by the definition of the magnetic vector potential $\vec{A}$ such that $\vec{B} = \nabla \times \vec{A}$. The integration in space of the Faraday-Lenz law relates the electric field strength $\vec{E}$ to the magnetic vector potential and to the electric scalar potential ϕ, i.e., $\vec{E} = -\frac{\partial}{\partial t}\vec{A} - \nabla\phi$. The current density $\vec{J}$ is related to the electric field strength by the anisotropic conductivity σ, i.e., $\vec{J} = \sigma\vec{E}$. The introduction of the potentials and material relations into Ampères law results in

$$\nabla \times \left(\nu \nabla \times \vec{A}\right) + \sigma\frac{\partial \vec{A}}{\partial t} = \vec{J}_{\mathrm{s}} \qquad (1)$$

with the reluctivity $\nu = 1/\mu$ and the source-current density $\vec{J}_{\mathrm{s}} = -\sigma\nabla\phi$.

We will consider two different methods for discretising (1). Both for the case of the Finite Integration Technique (FIT) as for the case of the lowest order Whitney Finite Element Method (FEM), the degrees of freedom are the magnetic vector potentials integrated along the primary edges of the computational grid, and are collected in the vector $\widehat{\mathbf{a}}$. The magnetic fluxes $\widehat{\widetilde{\mathbf{b}}}$ through the primary faces follow from applying the discrete curl operator at the primary grid, i.e., $\widehat{\widetilde{\mathbf{b}}} = \mathbf{C}\widehat{\mathbf{a}}$. A dual grid is constructed with the primary cell centers as dual grid points. The magnetic field strengths $\widehat{\mathbf{h}}$ integrated along the dual edges are related to the currents $\widehat{\widetilde{\mathbf{j}}}$ through the dual faces by $\widehat{\widetilde{\mathbf{j}}} = \widetilde{\mathbf{C}}\widehat{\mathbf{h}}$ where $\widetilde{\mathbf{C}}$ is the discrete curl operator defined at the dual grid. The divergence-freeness of the magnetic fluxes and the currents are represented on the discrete level by the expressions $\mathbf{S}\widehat{\widetilde{\mathbf{b}}} = 0$ and $\widetilde{\mathbf{S}}\widehat{\widetilde{\mathbf{j}}} = 0$ where $\mathbf{S}$ and $\widetilde{\mathbf{S}}$ are the discrete divergence operators at the primary and dual grid respectively. For topological reasons, the discrete gradient operators $\mathbf{G}$ and $\widetilde{\mathbf{G}}$ at both grids are related to the discrete divergence operators by $\mathbf{G} = -\widetilde{\mathbf{S}}^T$ and $\widetilde{\mathbf{G}} = -\mathbf{S}^T$ and both discrete curl operators are related by $\widetilde{\mathbf{C}} = \mathbf{C}^T$. The discrete material relations are expressed by $\widehat{\mathbf{h}} = \mathbf{M}_\nu\widehat{\widetilde{\mathbf{b}}}$ and $\widehat{\widetilde{\mathbf{j}}} = \mathbf{M}_\sigma\widehat{\mathbf{e}}$ where $\mathbf{M}_\nu$ is the reluctivity matrix and $\mathbf{M}_\sigma$ is the conductivity matrix.

* This work was supported by the Gesellschaft für Schwerionenforschung, Darmstadt and the Graduiertenkolleg "Technik und Physik von Beschleunigern" of the Deutsche Forschungsgemeinschaft (DFG).

The Finite Integration Technique and the Finite Element Method differ in the discretization of the material relations. For the Finite Integration Technique applied to an orthogonal hexahedral grid pair, the material matrices are diagonal. In a homogeneous region of the model, the entries

$$\mathbf{M}^{(fit)}_{\nu,q,q} = \nu \frac{|\tilde{L}_q|}{|S_q|} \tag{2}$$

of the reluctivity matrix discretize the relation between the magnetic flux $\widehat{\mathbf{b}}_q$ through the primary facet S_q to the magnetic voltage $\widehat{\mathbf{h}}_q$ along the dual edge $\tilde{L}_q$. The entries

$$\mathbf{M}^{(fit)}_{\sigma,j,j} = \sigma \frac{|\tilde{S}_j|}{|L_j|} \tag{3}$$

of the conductivity matrix relates the current $\widehat{\tilde{\mathbf{j}}}_j$ through the dual facet $\tilde{S}_j$ to the electric voltage $\widehat{\mathbf{e}}_j$ along the primary edge L_j. The material matrices used in the rest of the paper are slightly more general and allow non-homogeneous model regions and non-conforming grids. Their construction is described in [14] and [1].

In the case of the Finite Element Method, the degrees of freedom are expanded into the cells by the lowest-order Whitney edge functions $\vec{w}_j$. A compatible set of lowest-order facet functions $\vec{z}_q$ serves for discretising the magnetic flux. In general, the material matrices are not diagonal. Their entries are defined by

$$\mathbf{M}^{(\mathrm{fe})}_{\nu,p,q} = \int_\Omega \vec{z}_p \cdot \nu \vec{z}_q \, \mathrm{d}\Omega \; ; \tag{4}$$

$$\mathbf{M}^{(\mathrm{fe})}_{\sigma,i,j} = \int_\Omega \vec{w}_i \cdot \sigma \vec{w}_j \, \mathrm{d}\Omega \tag{5}$$

where Ω is the computational domain. The discretization of the source-current density reads

$$\widehat{\tilde{\mathbf{j}}}^{(\mathrm{fe})}_{\mathrm{s},i} = \int_\Omega \vec{w}_i \cdot \vec{J}_\mathrm{s} \, \mathrm{d}\Omega \; . \tag{6}$$

In the following, FE and FIT discretizations will be used equivalently. When differences appear in the construction of material matrices, superscripts "(fit)" and "(fe)" will be used.

For both approaches, the discrete counterpart of (1) reads

$$\widetilde{\mathbf{C}}\mathbf{M}_\nu \mathbf{C}\widehat{\mathbf{a}} + \mathbf{M}_\sigma \frac{d\widehat{\mathbf{a}}}{dt} = \widehat{\tilde{\mathbf{j}}}_\mathrm{s} \; . \tag{7}$$

Because $\mathbf{M}_\sigma$ has zero entries for the non-conductive regions, (7) is a system of differential-algebraic equations. The system is discretized in time by a four-stage singly diagonally implicit Runge-Kutta (SDIRK) method and requires the successive solution of four nonlinear systems of equations of the form

$$\left(\widetilde{\mathbf{C}}\mathbf{M}_\nu \mathbf{C} + \alpha \mathbf{M}_\sigma\right) \widehat{\mathbf{a}} = \mathbf{f} \tag{8}$$

where the particular SDIRK method determines the coefficient α and the construction of the righthandside $\mathbf{f}$ from $\widehat{\tilde{\mathbf{j}}}_\mathrm{s}$

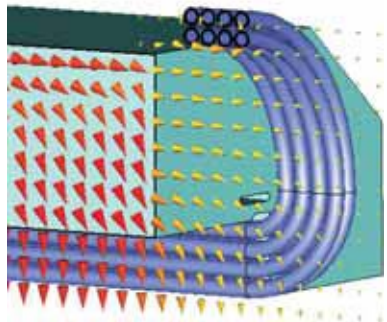

Figure 1: Magnetic flux at the end parts of the SIS-100 magnet.

and the solutions at the previous time steps. The ferromagnetic saturation in the yoke causes $\mathbf{M}_\nu(\widehat{\mathbf{b}})$ to depend on the magnetic fluxes $\widehat{\mathbf{b}} = \mathbf{C}\widehat{\mathbf{a}}$. The system (8) is linearized by the successive substitution approach.

HOMOGENISATION OF THE LAMINATED YOKE

To avoid eddy currents along the axial direction, here coinciding with the z-direction, the magnet yoke is laminated with respect to the z-direction. Nevertheless, in the end regions of the magnets, significant eddy-current effects are generated, especially due to the z-component of the magnetic flux (Fig. 1). The thickness of an individual lamination is 1 mm and therefore substantially smaller than the length of the magnet (more than 1 m). As a consequence, explicitly resolving individual laminations in the computational grid is not possible. Instead, the particular behavior of the laminated stack is represented by an equivalent homogeneous material. The laminated structure results in an anisotropy whereas the iron material causes the homogenized material to be nonlinear. The homogenized material is described by the anisotropic conductivity and reluctivity tensors $\overline{\overline{\sigma}} = \mathrm{diag}(\sigma_{xy}, \sigma_{xy}, 0)$ and $\overline{\overline{\nu}} = \mathrm{diag}(\nu_{xy}, \nu_{xy}, \nu_z)$ where the homogenized material parameters are

$$\sigma_{xy} = \gamma\sigma_\mathrm{Fe} \tag{9}$$

$$\frac{1}{\nu_{xy}} = \frac{\gamma}{\nu_\mathrm{Fe}} + \frac{1-\gamma}{\nu_\mathrm{ct}} \tag{10}$$

$$\nu_z = \gamma\nu_\mathrm{Fe} + (1-\gamma)\nu_\mathrm{ct} \tag{11}$$

where σ_Fe and ν_Fe are the conductivity and the reluctivity of the iron material, ν_ct is the reluctivity of the coating material and γ is the stacking factor. Because of the dependence of ν_Fe on the magnitude of the magnetic flux density, $\overline{\overline{\nu}}$ has to be updated in every nonlinear step. This homogenization approach is the rather rudimentary, but is sufficient to model the laminated structure up to a sufficient accuracy [7]. More elaborated homogenization schemes are described in e.g. [6].

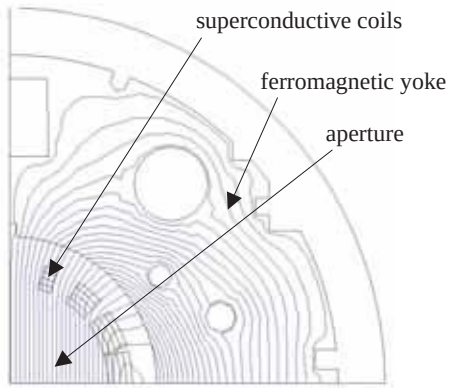

Figure 2: Dipole magnetic field in a $\cos\phi$-type magnet.

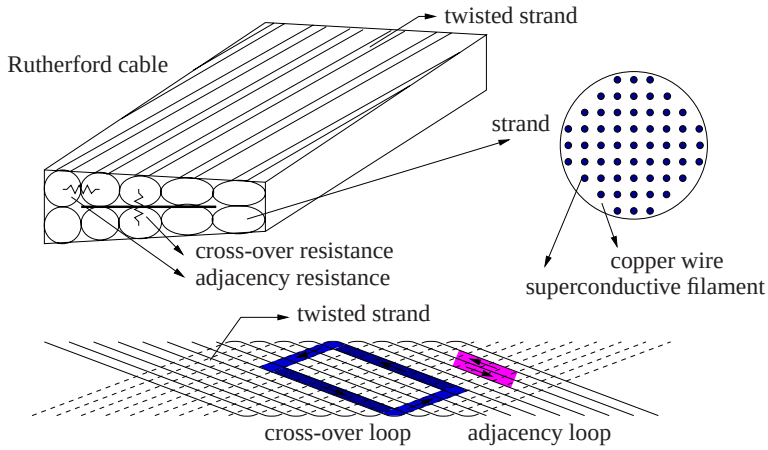

Figure 3: Geometry of a Rutherford cable.

HOMOGENISATION OF THE SUPERCONDUCTIVE COILS

Superconductive cable

The cable of a superconductive coil is typically a layered arrangement of strands which is sometimes transposed and keystoned in order to provide a good fit to the overall geometry (Fig. 2). Each strand is a copper wire in which superconductive filaments are embedded. The commercially available Rutherford cable consists of two transposed layers of strands with NbTi-filaments (Fig. 3). Unless the filaments are saturated or eddy currents appear, the entire current load flows through the superconductive filaments. Time-varying magnetic fields cause persistent currents in the filaments and coupling currents between several filaments inside the same copper wire [15]. These effects are typically modeled as a superconductive hysteresis effect [13]. The strand coating is of a limited resistance such that the current can redistribute in case of a quench and such that a sufficiently low thermal insulation is present [17]. Hence, time-varying magnetic fields incident to the superconductive cable also generate *inter-strand* or *cable* eddy currents which are migrating between different cable strands [11]. The insulation of the entire cable is of a substantially higher quality and prevents current migration between different turns of the coil. Resolving the individual strands and their insulation within an overall FE model of the device would lead to unacceptably large models due to the large differences in size between the device and the cable cross-sections. Therefore, the application of standard transient FE tools is not feasible in practice. Though occurring at microscopic scale, cable eddy-current effects can not be neglected in the simulation of ramped superconductive magnets. Here, homogenization techniques are presented which model the cable behavior up to a sufficient accuracy without requiring the cable geometry to be considered in full detail [3, 2].

Analytical cable eddy-current models

In analytical models, cable eddy-current effects are represented by a *cable magnetization*

$$M_s = -\tau_{\mathrm{cable}} \frac{d\vec{B}}{dt} \cdot \vec{e}_s \qquad (12)$$

which depends on the change of the incident magnetic field $\vec{B}$, a *cable time constant* τ_{cable} and the orientation of the current loop as represented by the normal vector $\vec{e}_s = (\cos\varphi_s, \sin\varphi_s)$ [15]. Analytical cable magnetization models relate the eddy-current magnetization directly to the change of the magnetic flux density and thus combine the laws of Faraday-Lenz and Ampère by relying upon a-priori knowledge of the eddy-current paths (Fig. 4). The cable time constant is measured or derived by analytically averaging the eddy-current effect over many current loops in the considered cable geometry [12]. For the example of Rutherford cables, two different kinds of cable eddy-current paths are distinguished: rectangular paths which consist of two neighboring strands and carry so-called *adjacency eddy currents*, and diamond-shaped paths which are formed by two strands of different layers and two cross-over points and carry *cross-over eddy currents* (Fig. 3). Both effects are characterized by their time constants τ_{pa} and τ_{pc} respectively.

Cable magnetization model

The cable eddy-current effects are modeled by a magnetising-current term

$$\nabla \times (\nu M_s \vec{e}_s) = \nabla \times \left(\nu \overline{\overline{\tau}} \nabla \times \frac{\partial \vec{A}}{\partial t} \right) \qquad (13)$$

rather than the eddy-current term $\sigma \frac{\partial}{\partial t}\vec{A}$ in (1) [5]. Here, $\overline{\overline{\tau}} = \tau_{\mathrm{pa}}\vec{e}_{\mathrm{pa}} : \vec{e}_{\mathrm{pa}} + \tau_{\mathrm{pc}}\vec{e}_{\mathrm{pc}} : \vec{e}_{\mathrm{pc}}$ denotes the anisotropic macroscopic time constant, combining the time constants τ_{pa} and τ_{pc} of the occurring cable eddy currents with the unit vectors $\vec{e}_{\mathrm{pa}}$ and $\vec{e}_{\mathrm{pc}}$ perpendicular to the corresponding

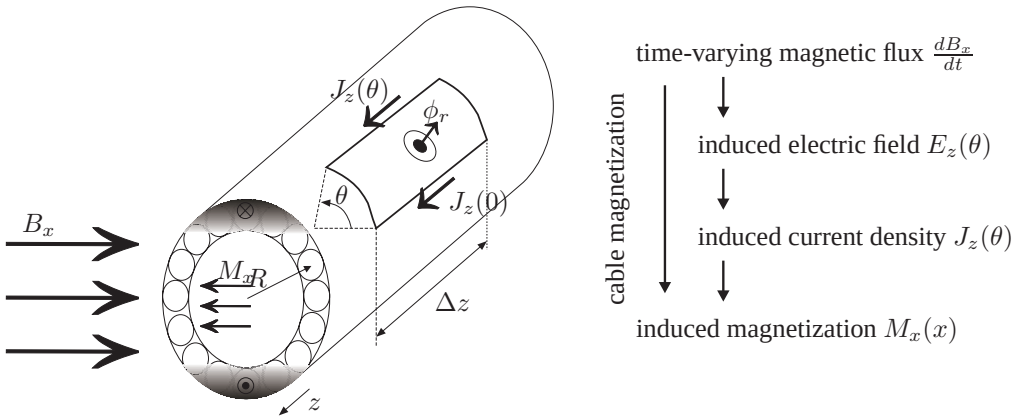

Figure 4: SIS-100 cable: current density J_z induced by a time-varying magnetic field B_x causing a magnetization M_x.

eddy-current paths. In the discrete setting of (7), $\mathbf{M}_\sigma \frac{d}{dt}\widehat{\mathbf{a}}$ is replaced by $\widetilde{\mathbf{C}}\mathbf{M}_{\nu\tau}\mathbf{C}\frac{d}{dt}\widehat{\mathbf{a}}$. The magnetization matrix $\mathbf{M}_{\nu\tau}$ is assembled similarly as in (2) and (4), e.g., in the FE case:

$$\mathbf{M}^{(\mathrm{fe})}_{\nu\tau,p,q} = \int_\Omega \vec{w}_p \cdot \nu\overline{\overline{\tau}}\vec{w}_q \,\mathrm{d}\Omega \,. \qquad (14)$$

Due to the anisotropic character of $\overline{\overline{\tau}}$, $\mathbf{M}_{\nu\tau}$ is non-diagonal, even for the FIT applied on an orthogonal grid pair. The cable magnetization model relies upon a few cable time constants determined by analytical models or by measurements, which may lead to inaccurate results.

Mixed cable eddy-current models

More accurate models for cable eddy-current effects have been proposed and discussed [5, 2, 4]. As resolving individual strands is impossible in practice, a homogenization of the complicated coil geometry has to be carried out. The model should allow for current redistribution at microscopic scale and prevent currents to couple between different cable turns, even when the insulation layers are not resolved by the mesh. The composite structure of the coil is modeled by an anisotropic conductivity $\overline{\overline{\sigma}}_{\mathrm{coil}}$. The winding direction $\vec{t}_{\mathrm{wind}}$, the short cross-sectional direction $\vec{t}_{\mathrm{short}}$ and the long cross-section direction $\vec{t}_{\mathrm{long}}$ are determined in all mesh cells inside the coil by the geometric modeler. The diagonal conductivity tensor $\overline{\overline{\sigma}}_{\mathrm{local}} = \mathrm{diag}(\sigma_{\mathrm{wind}}, \sigma_{\mathrm{short}}, \sigma_{\mathrm{long}})$ with respect to this local coordinate system is transformed into the global, spatially dependent conductivity tensor $\overline{\overline{\sigma}}_{\mathrm{global}} = \mathbf{R}^T\overline{\overline{\sigma}}_{\mathrm{local}}\mathbf{R}$ where $\mathbf{R}$ is the rotating operator between the local coordinate system and the global coordinate system. The conductivity related to the global coordinates is assembled into the conductivity matrix $\mathbf{M}_\sigma$ by the procedures defined by (3) and (5).

The anisotropic conductivity models the finite resistance between the parallel wires within the cable cross-section, but does not yet reflect the perfect insulation between the windings. The primary edges crossing insulation barriers are identified and their indices are collected in the set $\mathcal{S}$.

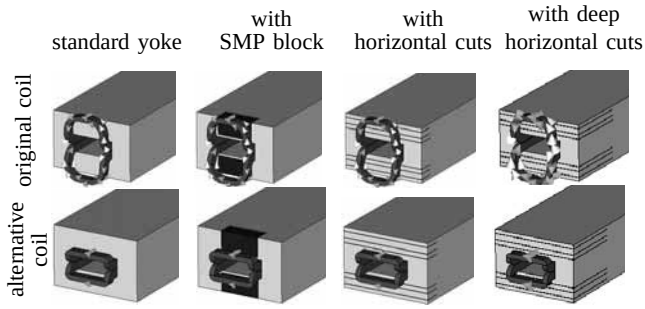

Figure 5: Eight considered magnet configurations.

A diagonal matrix $\mathbf{Z}$ is constructed such that $\mathbf{Z}_{e,e} = 0$ when $e \in \mathcal{S}$ and $\mathbf{Z}_{e,e} = 1$ when $e \notin \mathcal{S}$. The modified conductivity matrix $\mathbf{Z}\mathbf{M}_\sigma\mathbf{Z}$ accounts for the perfect inter-turn insulation. For the SIS-300 magnet, the set $\mathcal{S}$ is found by first cataloguing all primary nodes according to the coil turn in which they lay and then searching for all primary edges connecting nodes of different coil turns. If the mesh length is substantially larger than the thickness of the cable, the same procedure is carried out, but with fictitious turns with a larger cross-section.

RESULTS FOR THE SIS-100 MAGNET

A eighth of the SIS-100 magnet is modeled. The yoke has a stacking factor $\gamma_{\mathrm{stack}} = 0.98$ and a conductivity of $\kappa_{xy} = 3.2e6$ S/m. The ramping of the magnet and the end-winding parts cause the reluctivity of the iron to depend on both space and time. The simulations are carried out by a FIT model with approximately 30000 degrees of freedom (dofs) and one with approximately 100000 dofs. The eddy-current losses per cycle are 25.9 J and 22.7 J for the small and larger model respectively. The difference indicates that a very fine mesh is needed to obtain reliable results. Comparable results for the SIS-100 magnets are given in [9] and [8]. To study a possible reduction of the eddy-current losses by modifying the coil and the yoke, eight configurations are simulated (Fig. 5). Four config-

Table 1: Eddy-current losses per cycle, computed for a time step of 0.01 s and for two different discretizations

		small model (±30000 dofs)	large model (±100000 dofs)
original coil	standard yoke	25.9 J	22.7 J
	yoke with SMP block	18.7 J	19.3 J
	yoke with horizontal cuts	22.0 J	24.4 J
	yoke with deep horizontal cuts	21.2 J	22.8 J
alternative coil	standard yoke	7.67 J	8.03 J
	yoke with SMP block	5.17 J	6.69 J
	yoke with horizontal cuts	10.13 J	9.67 J
	yoke with deep horizontal cuts	8.79 J	9.14 J

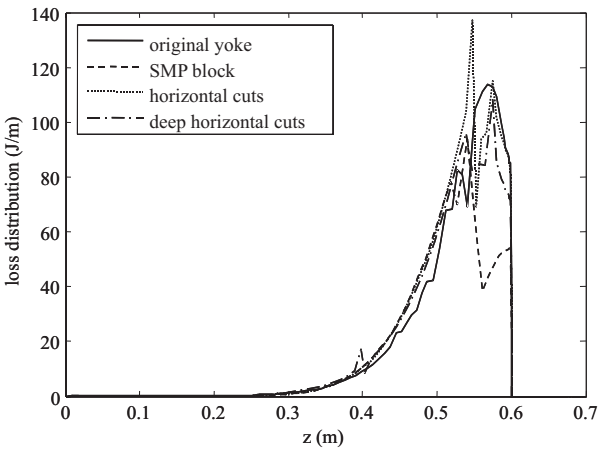

Figure 6: Eddy-current loss distribution along the axis of the magnet configurations with the original coil.

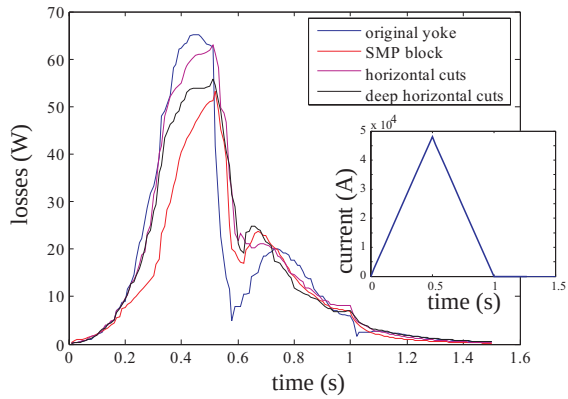

Figure 7: Eddy-current power losses during the cycling for the magnet configurations with the original coil.

urations feature the original coil (”original coil”) whereas the four other configurations are equipped with an alternative coil (”alternative coil”). Four yokes are considered: the ”standard yoke”, a yoke where a block of a sintered magnetic powder (SMP) material is inserted at the ends (”with SMP block”), a yoke where horizontal cuts with a depth of 50 mm are applied at the vertical positions (”with horizontal cuts”) and a yoke where horizontal cuts with a depth of 200 mm are applied at the same vertical positions (”with deep horizontal cuts”). Qualitative improvements of the different coil and yoke designs are clear from comparing the rows in Table 1. The differences for both computational grids (compare the columns in Table 1) indicate, however, that one has to be careful with quantitive conclusions. Both the SMP block and the horizontal cuts cause a reduction of the eddy-current losses, albeit less than one would expect. A modification to the coil has more effect. The spatial distribution of the eddy-current losses along the axis of the magnet is shown in Fig. 6. The SMP block shifts the eddy-current losses to the inside of the magnet. The horizontal cuts restrict some eddy-current paths and therefore also cause a reduction of the eddy-current losses. In theory, optimal cuts are organized such that they are parallel to the magnetic flux lines and orthogonal to the expected eddy currents. The time dependence of the eddy-current losses is shown in Fig. 7. The power losses are similar for the three yokes at the beginning of the cycling. First when saturation appears, differences in the magnitude of the power losses come up. The ferromagnetic saturation prevents large flux densities and therefore indirectly also prevents large eddy-current losses.

RESULTS FOR THE SIS-300 MAGNET

The cable magnetization model and the cable eddy-current model are used in combination with a magneto-quasistatic formulation discretized by the FIT in space and discretized by the SDIRK-3(2) method in time. The magnetizations computed by both approaches are compared in Fig. 8 for the case of cross-over eddy currents. The difference between Fig. 8a and Fig. 8b indicates that the cable magnetization model may be inaccurate and should be depreciated in favor of the cable eddy-current model. The double-layer structure of the coils is reflected in the cross-over and adjacency eddy-current distributions occurring in the Rutherford cable (Fig. 9). The cable eddy-current model implements barriers between the coil windings. Based on this simulation tool, the additional losses and the deterioration of the aperture field during the ramping of the superconductive magnets is computed.

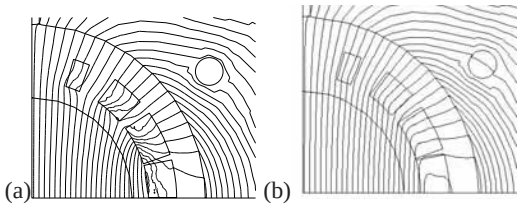

Figure 8: Magnetic flux lines of the magnetization of the $\cos\phi$-type dipole superconductive magnet due to cross-over eddy currents in the coils: (a) simulated by the cable magnetization model; (b) simulated by the cable eddy-current model.

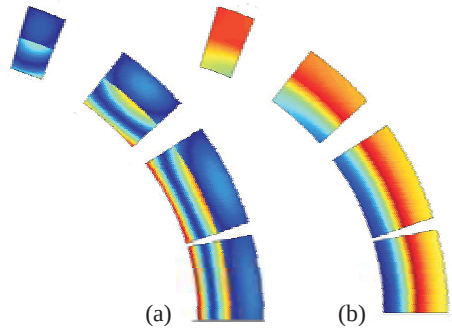

Figure 9: Distribution of (a) the adjacency eddy current density due to the time-varying azimuthal field and (b) the cross-over eddy current density in the Rutherford cable.

CONCLUSIONS

The laminated structure of the magnet yoke and the inner geometry of superconductive cable introduce geometrical details in superconductive magnet models which can not be resolved by the computational grid. It is possible to incorporate eddy-current effects in the yoke and cable composites when applying appropriate homogenization techniques. Then, it becomes possible to compute the aperture-field deterioration and the eddy-current losses due to the ramping of the magnets.

REFERENCES

[1] M. Clemens and T. Weiland. Magnetic field simulation using conformal FIT formulations. *IEEE Transactions on Magnetics*, 38(2):389–392, 2002.

[2] H. De Gersem, C. Mühle, M. Clemens, G. Moritz, and T. Weiland. Numerical simulation of eddy currents in the superconductive Rutherford cable of a fast-pulsed dipole magnet. In A. Andreone, G.P. Pepe, R. Cristiano, and G. Masullo, editors, *Proceedings of the 6th European Conference on Applied Superconductivity (EUCAS 2003), Sorrento, Italy, September 14-18, 2004*, number 181 in Applied Superconductivity, pages 1975–1982. Institut of Physics, 2004.

[3] H. De Gersem and T. Weiland. Finite element models for superconductive cables with finite inter-wire resistance. In *Proceedings of the XIVth Conference on the Computation of Electromagnetic Fields (COMPUMAG2003)*, volume 3, pages 64–65, Saratoga Springs, New York, USA, July 2003.

[4] H. De Gersem and T. Weiland. A finite element model for Rutherford cable in superconductive magnets. In W.H.A. Schilders, E.J.W. ter Maten, and S.H.M.J. Houben, editors, *Proceedings of the SCEE-2002 Conference, Eindhoven, the Netherlands, 23-28 June, 2002*, Scientific Computing in Electrical Engineering, Mathematics in Industry, Vol. 4, the European Consortium for Mathematics in Industry, pages 171–179. Springer, Berlin, 2004.

[5] H. De Gersem and T. Weiland. Finite-element models for superconductive cables with finite inter-wire resistance. *IEEE Transactions on Magnetics*, 40(2):667–670, March 2004.

[6] P. Dular, J. Gyselinck, C. Geuzaine, N. Sadowski, and J.P.A. Bastos. A 3D magnetic vector potential formulation taking eddy currents in lamination stacks into account. *IEEE Transactions on Magnetics*, 39(3):1424–1427, May 2003.

[7] H. Euler and T. Weiland. Zur Berechnung der Wirbelströme in beliebig geformten, lamellierten, dreidimensionalen Eisenkörpern. *Archiv für Elektrotechnik*, 61:103–109, 1979.

[8] E. Fischer, R. Kurnyshov, G. Moritz, and P. Shcherbakov. 3-D transient process calculations for fast cycling superferric accelerator magnets. *IEEE Transactions on Applied Superconductivity*, 16(2):407–410, June 2006.

[9] A. Kalimov, E. Fischer, G. Hess, G. Moritz, and C. Mühle. Investigation of the power losses in a laminated dipole magnet with superconductive coils. *IEEE Transactions on Applied Superconductivity*, 14(2):267–270, June 2004.

[10] G. Moritz and et al. Towards fast-pulsed superconductive synchrotron magnets. In *PAC'2001*, Chicago, Illinois, USA, June 2001.

[11] R. Otmani, A. Devred, and P. Tixador. Interstrand and AC-loss measurements on Rutherford-type cables for accelerator magnet applications. *IEEE Transactions on Applied Superconductivity*, 11(1), March 2001.

[12] A.P. Verweij and H.H.J. ten Kate. Coupling currents in Rutherford cables under time varying conditions. *IEEE Transactions on Applied Superconductivity*, 3(1):146–149, March 1993.

[13] C. Völlinger, M. Aleksa, and S. Russenschuck. Calculation of persistent currents in superconductive magnets. *COMPEL*, 20(2):562–569, 2001.

[14] T. Weiland. Time domain electromagnetic field computation with finite difference methods. *International Journal of Numerical Modelling*, 9(4):295–319, July-August 1996.

[15] M.N. Wilson. *Superconductive Magnets*. Clarendon Press, Oxford, 1983.

[16] M.N. Wilson. Superconducting magnets for accelerators: a review. *IEEE Transactions on Applied Superconductivity*, 7(2):727–732, June 1997.

[17] M.N. Wilson and R. Wolf. Calculation of minimum quench energies in Rutherford cables. *IEEE Transactions on Applied Superconductivity*, 7(2):950–953, June 1997.